



저작자표시-비영리-변경금지 2.0 대한민국

이용자는 아래의 조건을 따르는 경우에 한하여 자유롭게

- 이 저작물을 복제, 배포, 전송, 전시, 공연 및 방송할 수 있습니다.

다음과 같은 조건을 따라야 합니다:



저작자표시. 귀하는 원저작자를 표시하여야 합니다.



비영리. 귀하는 이 저작물을 영리 목적으로 이용할 수 없습니다.



변경금지. 귀하는 이 저작물을 개작, 변형 또는 가공할 수 없습니다.

- 귀하는, 이 저작물의 재이용이나 배포의 경우, 이 저작물에 적용된 이용허락조건을 명확하게 나타내어야 합니다.
- 저작권자로부터 별도의 허가를 받으면 이러한 조건들은 적용되지 않습니다.

저작권법에 따른 이용자의 권리는 위의 내용에 의하여 영향을 받지 않습니다.

이것은 [이용허락규약\(Legal Code\)](#)을 이해하기 쉽게 요약한 것입니다.

[Disclaimer](#)

Thesis for the Degree of Master of Science

**A numerical study on the
characteristics of flow and dispersion of
pollutants in an urban area
using WRF-CFD**



by

A-Rum Kwon

Department of Environmental Atmospheric Sciences

The Graduate school

Pukyong National University

February 26, 2016

A numerical study on the characteristics
of flow and dispersion of pollutants
in an urban area using WRF-CFD
(WRF-CFD 접합 모델을 이용한
도시지역의 상세 흐름 및 오염물질
확산 특성 연구)

Advisor: Prof. Jae-Jin Kim

by

A-Rum Kwon

A thesis submitted in partial fulfillment of the requirements
for the degree of

Master of Science

in Department of Environmental Atmospheric Sciences,
The Graduate School,
Pukyong National University

February 2016

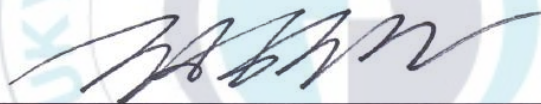
A numerical study on the characteristics of flow and dispersion
of pollutants in an urban area using WRF-CFD

A dissertation

by

A-Rum Kwon

Approved by:



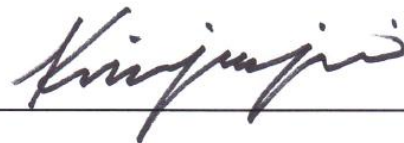
(Chairman)

Hyeong-Bin Cheong



(Member)

Won-Sic Choi



(Member)

Jae-Jin Kim

February 26, 2016

Contents

List of Figures	ii
List of Tables	v
Abstract	vi
1. Introduction	1
2. Methodology	5
2.1. Object area	5
2.2. Experimental set up	10
2.2.1. WRF-Chem (ver. 3.6) model	10
2.2.2. CFD model	13
3. Results	18
3.1. Wind fields analysis	18
3.2. Concentration fields analysis	32
4. Summary and conclusions	43
REFERENCE	47

List of Figures

Fig. 1. The satellite picture for the object area in Yeongdeungpo-gu, Korea (from http://map.naver.com).	6
Fig. 2. Wind roses of measured wind directions and speeds at AWS during experiment period (00KST 17 to 00KST 24 May, 2014).	8
Fig. 3. (a) Time series of measured wind directions and (b) wind speeds at AWS and (c) measured CO concentrations at AQMS.	9
Fig. 4. Domain configuration of WRF-Chem model.	12
Fig. 5. (a) Three and (b) two-dimensional configurations of buildings and topography for the object area in WRF-CFD simulations. The yellow and red circles represent AWS and AQMS, respectively.	14
Fig. 6. Time series of CO concentrations of on-road mobile source in the object area.	16
Fig. 7. (a) Three and (b) two-dimensional configurations of topography for the object area in WRF-Chem simulations. The yellow and red circles represent AWS and AQMS, respectively.	17
Fig. 8. (a) Time series of measured and simulated wind directions and (b) wind speeds at AWS. Black circles, grey triangles and dark grey squares represent measurements, WRF-Chem and WRF-CFD simulations, respectively.	20
Fig. 9. The degree of scattering for wind direction of inflow and the deceleration rate between WRF-Chem and WRF-CFD simulations at AWS.	23

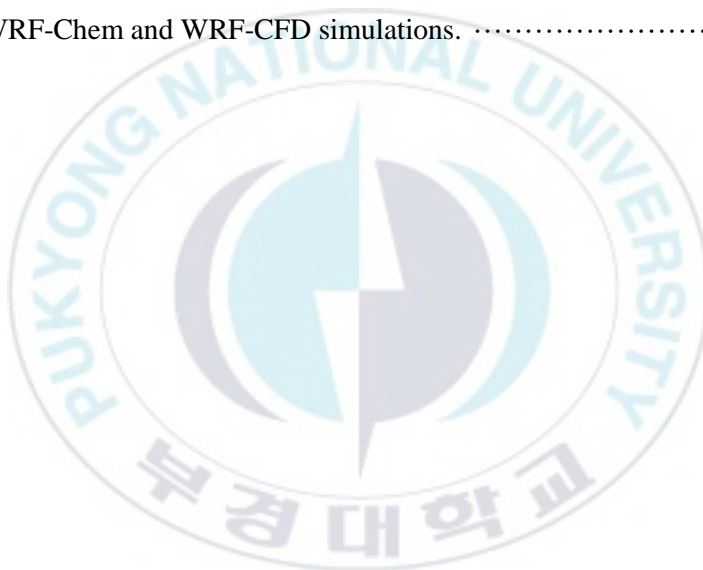
Fig. 10. Wind vectors ($\sqrt{U^2 + V^2}$) and contours of vertical wind (W) components at $z = 32.5$ m at 12 KST 20 May. A rectangle with red solid line represents region of (b) and red circles represent location of AWS.	25
Fig. 11. The same as in Figure 10 except for the 17 KST 17 May case.	27
Fig. 12. The same as in Figure 10 except for the 21 KST 20 May case.	29
Fig. 13. The same as in Figure 10 except for the 21 KST 23 May case.	31
Fig. 14. (a) Time series of measured and simulated CO concentrations, (b) simulated wind speeds ($\sqrt{U^2 + V^2}$) and (b) vertical wind (W) components. Black circles, white diamond, grey triangles and dark grey squares represent measurements, background CO concentrations, WRF-Chem and WRF-CFD simulations, respectively.	34
Fig. 15. The contours of CO concentration in a vertical plane around AQMS. White circle represent AQMS.	35
Fig. 16. (a) The degree of scattering between the simulated CO concentrations in WRF-CFD and CO emissions and (b) time.	36
Fig. 17. (left panels) Wind vectors ($\sqrt{U^2 + V^2}$) and contours of vertical wind (W) components and (right panels) contours of CO concentration at $z = 27.5$ m at 18 KST 22 May. Red rectangles represent region of (c) and (d) and red circles represent location of AQMS.	38
Fig. 18. The wind vector and contours of CO concentration in a vertical plane at street canyon.	39
Fig. 19. The same as in Figure 15 except for the 15 KST 22 May case.	41

Fig. 20. The same as in Figure 15 except for the 04 KST 22 May case. 42



List of Tables

Table 1. WRF-Chem model set-up for the simulations.	11
Table 2. The root mean square errors (RMSEs) of simulated wind directions and speeds in WRF-Chem and WRF-CFD simulations.	21
Table 3. The root mean square errors (RMSEs) of simulated CO concentrations in WRF-Chem and WRF-CFD simulations.	33



WRF-CFD 접합 모델을 이용한
도시지역의 상세 흐름 및 오염물질 확산 특성 연구

권아름

부경대학교 대학원 환경대기과학과

요 약

본 연구에서는 서울시 영등포구 지역의 상세 대기 흐름 및 오염 물질 확산 특성 분석을 위한 연구를 수행하였다. 영등포구 지역은 서울의 다른 지역에 비해 도시지역의 특징을 잘 반영하고 있는 지역으로, 도시지역에서 나타나는 상세 대기 흐름 및 오염물질의 확산 분석에 적합하다. 도시 지역에서 배출되는 다양한 오염물질 중 다른 오염물질과의 반응성이 거의 없고 자동차와 같은 도로이동오염원으로부터 주로 배출되는 일산화탄소(CO)를 대상으로 수치실험을 수행하였다. 수치 모의 실험 결과의 정밀도 향상을 위해 WRF-Chem 모델과 CFD 모델의 일 방향 접합모델(WRF-CFD 모델)을 사용하였다. WRF-CFD 모델을 이용한 수치 모의 실험에서는 WRF-Chem 모델의 모의 바람장과 농도장이 WRF-CFD 모델의 유입경계자료로 사용된다. 수치 모의 실험 결과, 두 모델 모의 풍향은 관측과 유사하였다. 하지만 두 모델 모두 풍향의 급격한 변화는 잘 모의하지 못하였다. 풍속의 경우, WRF-Chem 모델의 모의 풍속은 상세 지형과 건물 자료를 고려할 수 없기 때문에, WRF-Chem 모델의 모의 풍속은 관측 풍속에 비해 크게 과대모의 되었다. 반면에 WRF-CFD 모델은 상세 지형 및 건물 자료를 고려할 수 있으므로, WRF-CFD 모델의 모의 풍속은 관측 풍속과 유사하게 나타났다. 두 모델의 모의 풍향과 풍속을 비교해 본 결과, 유입류 풍속(WRF-CFD 모델의 모의 풍속) 대비 WRF-CFD 모델의 모의 풍속의 감률은 유입류 풍향에 따라 다르게 나타남을 알 수 있었다. 이를 분석하기 위해 풍향을 4가지 풍향(동, 서, 남, 북)으로 나누었다. 풍향이 동, 서 또는 북인 경우, AWS 주변에 흐름에 영향을 미칠만한 건물이 존재하기 때문에 풍속의 감률이 높게 나타났다. 반면에, 풍향이 남인 경우, AWS 남쪽에는 흐름에 영향을 미

철만한 건물이 존재하지 않기 때문에 풍속의 감률이 적게 나타났다. 이를 통해 WRF-CFD 모델은 건물에 의한 흐름변화를 잘 반영할 수 있음을 알 수 있었다. 대상 지역의 상세 오염물질 확산 분석을 위하여 앞서 모의된 각 모델의 바람장을 토대로 오염물질 확산 수치 실험을 수행하였다. 수치 실험을 위하여 초당 단위면적에서 배출되는 CO의 배출량을 산정하여 WRF-CFD 모델의 입력자료로 사용하였으며, 배경 농도장으로는 WRF-Chem 모델의 CO 농도장이 사용되었다. WRF-Chem 모델의 바람장을 이용한 경우, 관측 값에 비해 농도가 크게 과소 모의되었다. 이는 WRF-Chem 모델의 연직 속도성분이 수평 속도에 비해 약해 연직확산이 활발하게 일어나지 못했기 때문이다. WRF-CFD 모델의 바람장을 이용한 경우, 적은 CO 배출량으로 인해 낮은 CO 농도가 모의되는 야간(00시 - 05시)을 제외하고는 관측 CO 농도와 유사한 농도가 모의되었다. 오염물질 확산 특성 분석을 위하여 출퇴근 시간, 주간, 야간으로 나누어 분석을 수행하였다. CO 배출량이 많은 출퇴근 시간에는 높은 농도가 모의되었고, 배출량이 적은 야간에는 낮은 농도가 모의되었다. 주간에는 CO 배출량은 높지만 강한 모의 풍속으로 인해 농도 확산이 활발하기 때문에 출퇴근 시간에 비해 낮은 농도가 모의되었다. 본 연구에서는 WRF-Chem 모델과 CFD 모델의 일 방향 접합모델(WRF-CFD 모델)을 통해 상세 대기 흐름 및 오염물질의 확산의 정밀도를 향상시켰다. 이는 도시 지역 내의 대기 흐름에 따른 고농도 지역 파악에 용이하므로 이를 이용한 효율적인 대기질 모니터링 위치 선정이 가능하다. 또한 대기질 개선을 위한 방안 및 도시계획이나 재개발 계획 단계에서 쾌적한 대기환경 조성을 위한 가이드라인 제시가 가능하다.

1. Introduction

Airflow and pollutants dispersion in urban areas are very closely related to human lives. As the result of the industrialization, modernization and urbanization of several areas, numerous buildings including apartment complexes are constructed densely in urban areas. Buildings are one of the major factors that affect airflow and pollutants dispersion. The physical characteristics of buildings such as height, size and shape complicate airflow and pollutants dispersion (Ai and Mak, 2013; Kwak et al., 2014; Montazeri et al., 2015). Airflow and pollutants dispersion affect us directly or indirectly in an urban area that provides both home and work place for the human. Because of such significance, many studies for airflow and pollutants dispersion have been actively conducted (Bohnenstengel et al., 2014; Rakowska et al., 2014; Zheng et al., 2014).

The combined characteristics of the buildings are major factor that determines the airflow in an urban area. To analyze such airflow, a model such as CFD model that considers detailed topography and building information is required to perform calculations for a high-resolution in order to understand the changes of airflow in an urban area. CFD model uses detailed topography

and building information as surface boundary data in the model. The model calculates for the resolution of tens of meters or less and considers meteorological elements such as wind, temperature and humidity. Therefore, CFD model is frequently used in studies for airflow and pollutants dispersion in an urban area (Kwak et al., 2014; Kwon and Kim, 2014; Kwon and Kim, 2015).

An urban area is consisted of numerous street canyons. Street canyon means the spaces between buildings. The analysis of airflow and pollutants dispersion in street canyon is important to understand airflow and pollutants dispersion in an urban area. Many Studies have been conducted to analyze airflow and pollutants dispersion in street canyons (Tominaga and Stathopoulos, 2011; Baik et al., 2012; Kwak and Baik, 2012; Habilomatis and Chaloulakou; 2015). Such studies are suitable for analysis of dynamics and chemical process. However, such studies are not suitable in many urban areas where buildings with varying height, size and shape are lined up consecutively. Many studies have been conducted for analysis of airflow and pollutants dispersion in an urban area (Gousseau et al., 2011; Miao et al., 2013; Zheng et al., 2015).

Pollutants dispersion is the most significant factor of urban air quality. The spatial variability of air quality is mainly affected by local emission

sources (Clapp and Jenkin, 2001; Jenkin, 2004). Particularly on-road mobile emission sources are one of the most important local emission sources in urban areas where heavy traffic is constant (Zavala et al., 2006; Zhang and Ying, 2011; Masiol et al., 2012; Rissler et al., 2012). Many measurement studies have reported that concentrations of pollutants measured near roads are significantly higher than the urban background concentrations (Karner et al., 2010; Shon et al., 2011; Vette et al., 2013). Carbon monoxide (CO) is one of the pollutants contributing to urban air quality. CO has a negative effect on the human health as well as air quality itself. CO is a colorless and odorless gas formed by the incomplete combustion of fossil fuels (CLA, 2013). Vehicle exhaust accounts for the majority of CO emissions in urban areas. CO concentrations follow the spatial and temporal distributions of the traffic volume because CO is less reactive pollutant and its lifetime (2 - 3 month) is relatively longer than other primary pollutants such as NO_x and VOC (Fuglestedt et al, 1996). High CO concentrations are frequently observed in areas with heavy traffic. In terms of health, CO denatures hemoglobin, which carries oxygen to various parts of the body, into carbonyl hemoglobin, resulting reduced oxygen transport ability of blood. (Maeng and Heo, 2002; LSDCC, 2003). Exposure to high CO concentrations may cause carbon monoxide poisoning with symptoms of headache, tinnitus and dizziness, which may be further developed into lethargy,

coma, seizure and respiratory paralysis if the exposure is continued. Carbon Monoxide poisoning may lead to death in severe cases. As CO is extremely harmful pollutant to humans, many studies to predict the dispersion of CO have been actively conducted (Kim et al., 2012; Amirjamshidi et al., 2013; Li et al., 2015).

CFD model has been used to simulate non-reactive pollutants dispersion in many studies (Gousseau et al., 2011; Miao et al., 2013; Zheng et al., 2015). Background concentration is required to analyze non-reactive pollutants dispersion using CFD model. However, it is not involved in CFD model. Some studies use simulated data from mesoscale dispersion model, such as Weather Research and Forecasting model coupled with Chemistry (WRF-Chem) and Congestion Mitigation and Air Quality (CMAQ) model, to define initial boundary condition in CFD model (Kawk et al., 2014).

In this study, airflow and pollutant (CO) dispersion in an urban area are analyzed using CFD model coupled with WRF-Chem model (WRF-CFD model). CO is assumed to be non-reactive pollutant because it is less reactive pollutant in this study. The study consists of four chapters. The second chapter describes the methodology of this study such as the object area and experimental set up and the third chapter describes an analysis of airflow and pollutants dispersion. The last chapter describes the conclusion of this study.

2. Methodology

2.1. Object area

Yeongdeungpo-gu, Seoul, Korea was selected as the object area (Fig. 1) to analyze the dispersion of non-reactive pollutants (CO). The object area is suitable for analysis of airflow and CO dispersion because it reflects well the characteristics of an urban area.

The object area includes numerous buildings with various heights, sizes and shapes that complicate airflow. The building density of the area is higher than other urban areas in Seoul. The trees cause the change of airflow, but it is difficult to be simulate in CFD model. In the object area, the influence of trees is negligible because of the lack of trees. A river is located in the northwest and another river and wetland are located in the northeast of the object area. An automatic weather station (AWS) and air quality monitoring station (AQMS) are installed and operated in the object area. AWS is located in Seoul Youngdong elementary school. Meteorological data obtained from AWS

represents weather of Yeongdeungpo-gu. High apartment complexes are located around AWS. AQMS is located on the roof of Dangsang 1-dong Community Service Center. High apartment complexes are also located around AQMS and small-scale park is located in the west of AQMS.

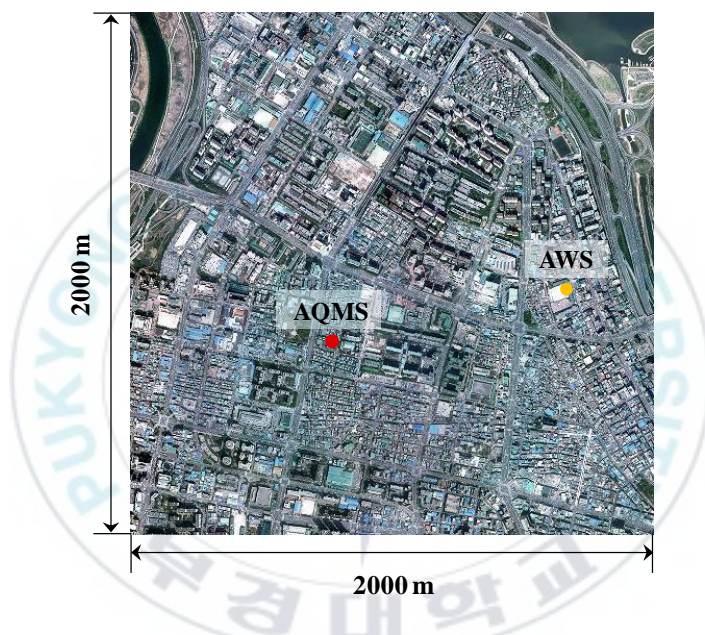


Fig. 1. The satellite picture for the object area in Yeongdeungpo-gu, Korea (from <http://map.naver.com>).

The simulations were performed for the period from 00 KST 17 to 00 KST 24 May 2014. The amount of pollutants emitted into the air from the heating is negligible in May due to warm weather. In summer (June to August), although pollutants from the heating are also negligible, wind speed is lower

than spring (March to May) and there are greater tendencies of having cloudy and rainy days. Therefore the experiment period, the last month of spring season, is more suitable to analyze airflow and dispersion of pollutants than other seasons. For this period (00 KST 17 to 00 KST 24 May 2014), sunny days without dust or rain were continued. South-southwesterly (20.83%) and southwesterly (17.26%) were frequent (Fig. 2 and 3a). The highest wind speed at AWS was 3 m s^{-1} at 17 KST 22 and 13 KST 23 May and the lowest wind speed was 0.5 m s^{-1} at 22 KST 22 and 00 KST 23 May (Fig. 3b). The mean wind speed was 1.64 m s^{-1} . The highest CO concentration was 1.1 ppm at 03KST 18 and 07 KST 23 May and the lowest CO concentration was 0.3 ppm (Fig. 3c). The mean CO concentration was 0.61 ppm. The wind speed and CO concentration represented inverse correlation that when wind speed was high, CO concentration was low.

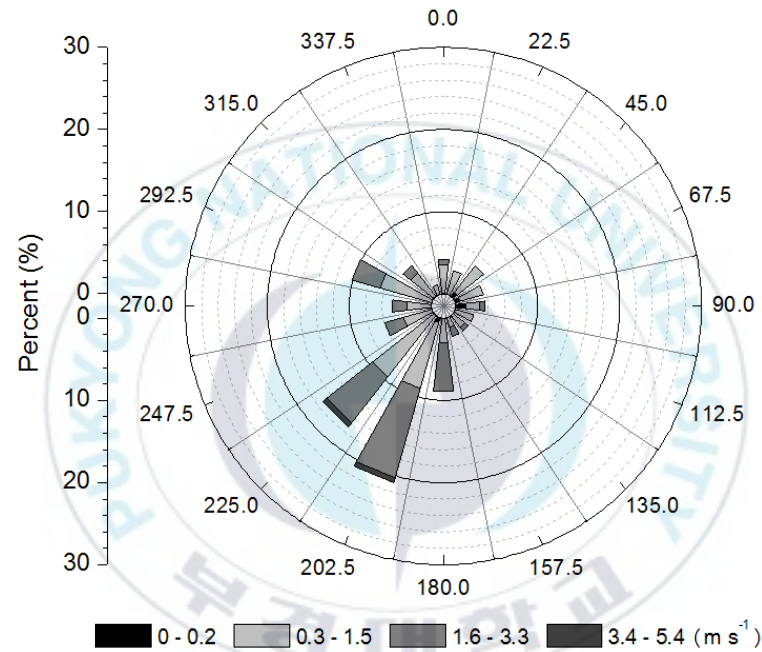


Fig. 2. Wind roses of measured wind directions and speeds at AWS during experiment period (00KST 17 to 00KST 24 May, 2014).

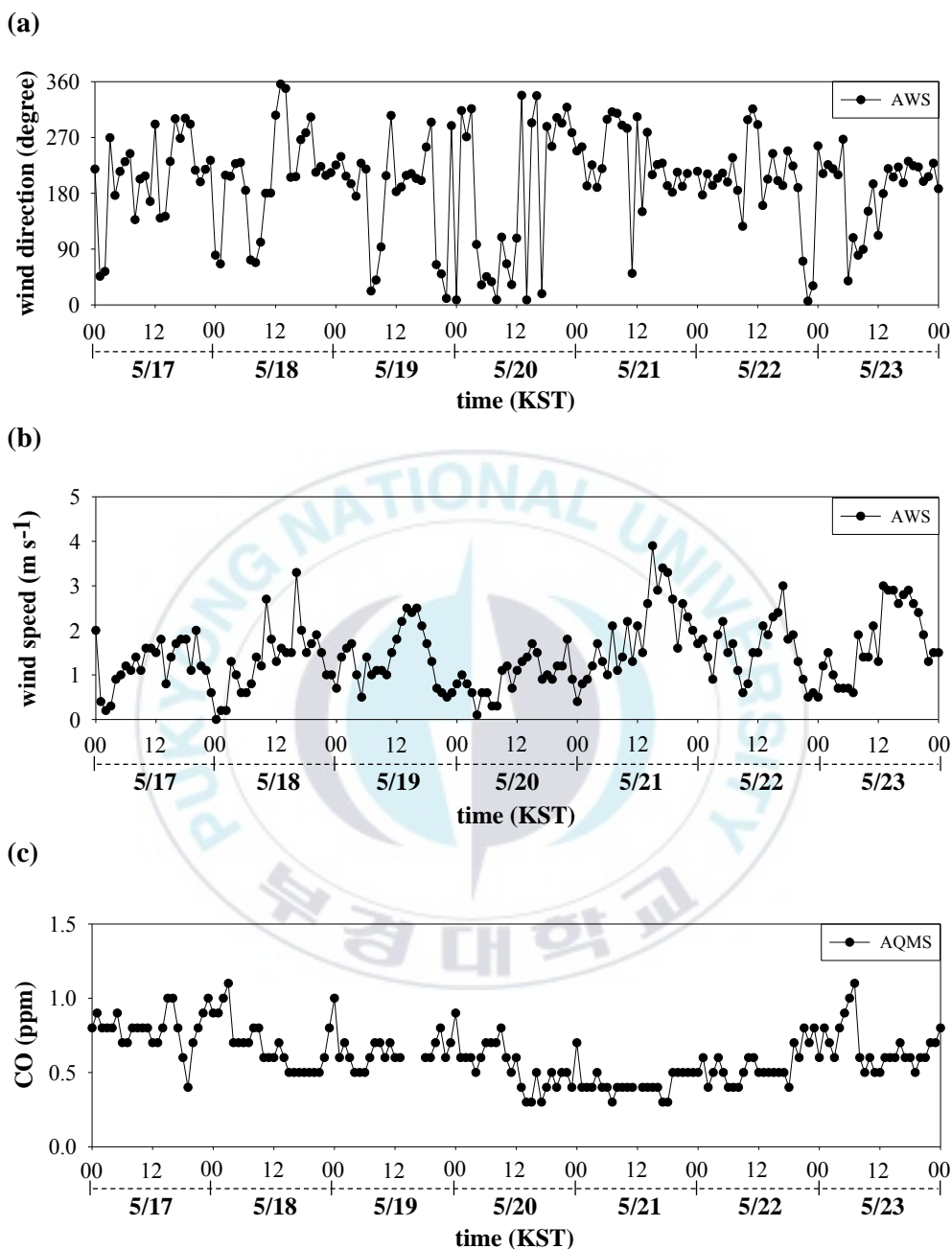


Fig. 3. (a) Time series of measured wind directions and (b) wind speeds at AWS and (c) measured CO concentrations at AQMS.

2.2. Experimental set up

2.1.1. WRF-Chem (ver. 3.6) model

In this study, CFD model coupled with WRF-Chem model (WRF-CFD model) was used to simulate airflow and pollutant dispersion in the object area. One-way coupling was used. WRF-Chem model simulates the chemical transformation of trace gases, mixing, transport, emissions and aerosols simultaneously with the meteorology. A horizontal resolution of mother domain (d01) in WRF-Chem model is $45\text{ km} \times 45\text{ km}$ with 27 eta levels. The domain was nested twice. Horizontal resolutions of other domains are $15\text{ km} \times 15\text{ km}$ (d02) and $3\text{ km} \times 3\text{ km}$ (d03), respectively. The model domains are shown Figure 4. Physics and chemical modules in WRF-Chem model were used to simulate meteorology and chemistry, as shown in Table 1.

The meteorological fields were simulated from d01 to d03. The $1^\circ \times 1^\circ$ final operational global final analysis (FNL) data, produced by the National Centers for Environmental Prediction (NCEP) every 6 hours, was used as initial and lateral boundary conditions for the meteorological simulations. The Mellor-Yamada-Janjic PBL scheme was used to calculate turbulent mixing at

surface and within boundary layers (Janjic, 1990; Janjic, 1994).

Table 1. WRF-Chem model set-up for the simulations.

Feature	Set-up
Initial/boundary conditions	NCEP final analysis data (6-h intervals, $1^{\circ} \times 1^{\circ}$ resolution)
Domain	d01 45 km grid with 27 layers
	d02 15 km grid with 27 layers
	d03 3 km grid with 27 layers
Microphysics scheme	WSM-3
Radiation scheme	RRTM long-wave / Dudhia short-wave
Surface layer physics	Monin-Obukhov
Land surface model	Noah LSM
Boundary layer	Mellor-Yamada-Janjic (MYJ) PBL scheme
Emission	SMOKE-Asia (only anthropogenic)
Chemical mechanism	CBMZ

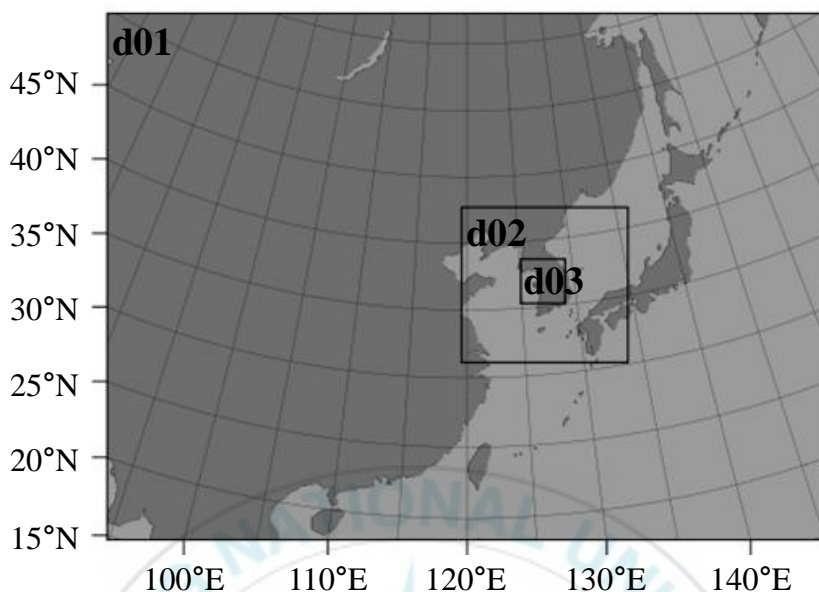


Fig. 4. Domain configuration of WRF-Chem model.

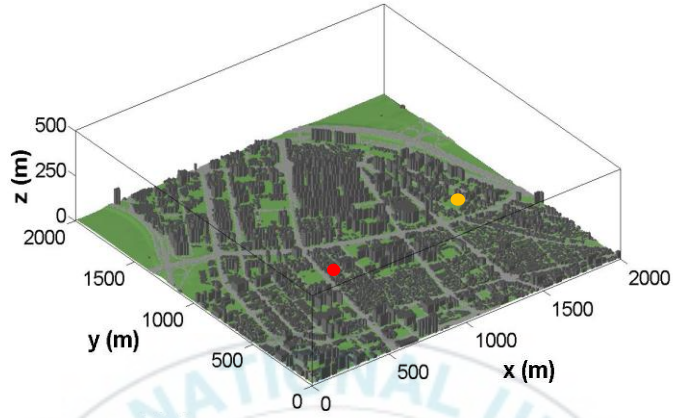
The chemical fields were simulated in d01 and only anthropogenic emission data from Sparse Matrix Operator Kernel Emission-Asia (SMOKE-Asia) developed by Woo et al. (2012) was used. The carbon bond mechanism Z (CBMZ) chemical mechanism was used to simulate CO concentrations (Zaveri and Peters, 1999). The chemical mapping data developed by Park et al. (2014) was used because the CBMZ mechanism differs from the carbon bond 05 (CB05) chemical mechanism using in SMOKE-Asia. Fast-J photolysis scheme was used to simulate photolysis reaction between chemical species (Wild et al., 2000; Barnard et al., 2004).

2.1.1. CFD model

CFD model used in this study is the same as Kim et al. (2014)'s model. The model simulates wind, temperature and concentration of non-reactive pollutants in urban area. The model is based on Reynolds Averaged Navier-Stokes (RANS) equation system and assumes a three-dimensional, non-rotating, non-hydrostatic and incompressible airflow system. RNG k- ϵ turbulence closure scheme (Yakhot et al., 1992) and Versteeg and Malalasekera (1995)'s wall function are applied. The governing equation system in the model is numerically solved on a staggered grid system using a finite volume method and the semi-implicit method for a pressure-linked equation (SIMPLE) algorithm suggested by Patankar (1980).

Numerical simulations using WRF-CFD model were performed for analysis of detailed airflow and CO dispersion in the object area. A domain size and cell size are $2000\text{ m} \times 2000\text{ m} \times 500\text{ m}$ and $10\text{ m} \times 10\text{ m} \times 5\text{ m}$ in x-, y- and z-direction, respectively (Fig. 5a and 5b). The simulated data in WRF-Chem simulations were interpolated according to the domain size which refers to the initial boundary condition of WRF-CFD model. WRF-CFD simulations were integrated for 3600 s with a time step of 0.5 s. Only CO data in WRF-

(a)



(b)

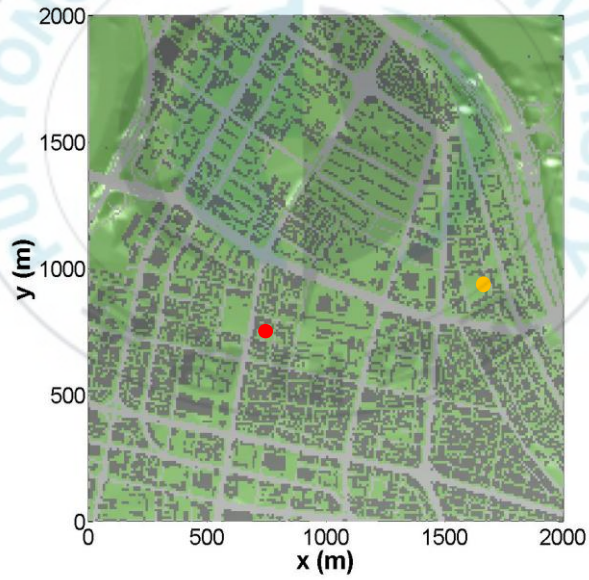


Fig. 5. (a) Three and (b) two-dimensional configurations of buildings and topography for the object area in WRF-CFD simulations. The yellow and red circles represent AWS and AQMS, respectively.

Chem simulations was used as the background concentration and only the on-road mobile emission source were considered. The emission of on-road mobile source was calculated in Eq. (1).

$$E = \frac{E_d}{A_r} \times EF_m \times EF_d \times EF_t \times \frac{1}{3600 \text{ s}} \quad (1)$$

where, E means the CO emission of on-road mobile source ($\text{kg m}^{-2} \text{ s}^{-1}$) in the object area, E_d means daily mean the CO emission (kg day^{-1}), A_r means area of roads in the object area (m^2) and EF_m , EF_d and EF_t mean the monthly, daily and timely emission coefficients, respectively. Figure 6 shows the CO emissions during experiment period. The CO emission was low ($< 0.5 \times 10^{-5} \text{ kg m}^{-2} \text{ s}^{-1}$) during 01 KST to 05 KST and was highest ($1.48 \times 10^{-5} \text{ kg m}^{-2} \text{ s}^{-1}$) at 08 KST 17 May. The mean CO emission was $0.98 \times 10^{-5} \text{ kg m}^{-2} \text{ s}^{-1}$ during experiment period.

For comparison with WRF-CFD simulations, CO dispersion simulations were performed using simulated wind data in WRF-Chem simulations. The CO data in WRF-Chem simulations and CO emissions were used, same way as WRF-CFD simulations. The numerical experiments were simulated using numerical domain (Fig. 7) that does not involve buildings because WRF-Chem model doesn't consider effect of buildings. The model

was integrated for 3600 s with a time step of 0.5 s.

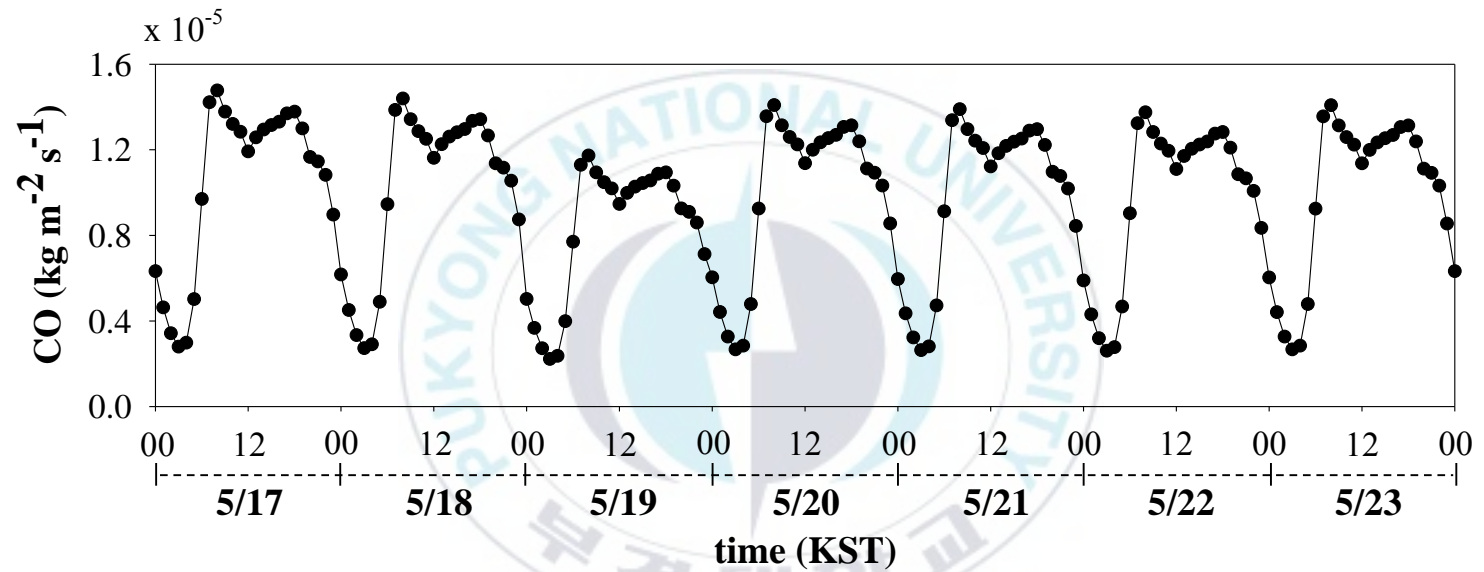
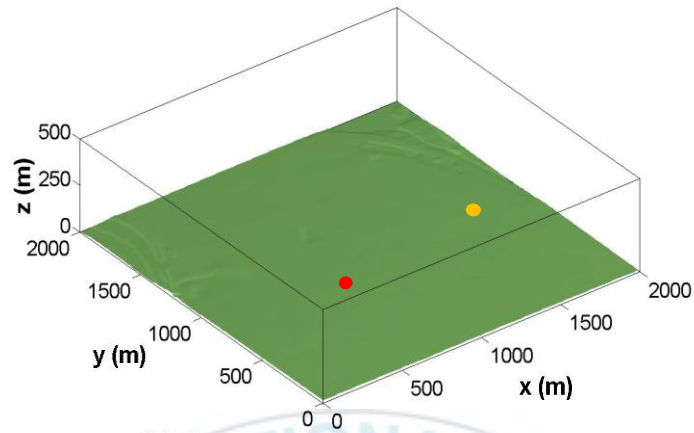


Fig. 6. Time series of CO emissions of on-road mobile source in the object area.

(a)



(b)

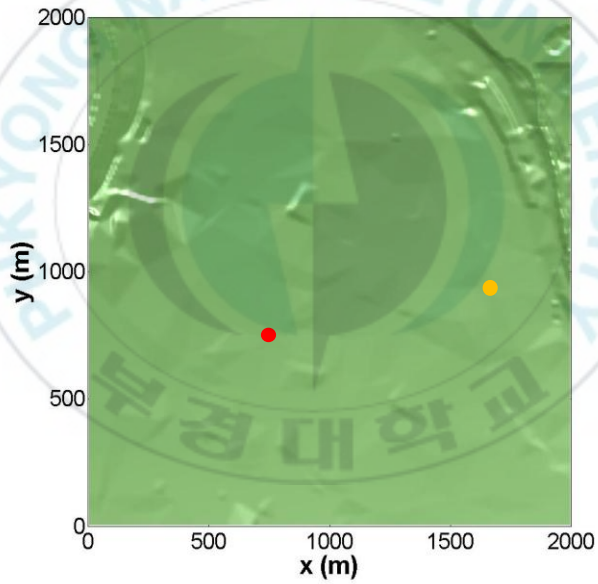


Fig. 7. (a) Three and (b) two-dimensional configurations of topography for the object area in WRF-Chem simulations. The yellow and red circles represent AWS and AQMS, respectively.

3. Results

3.1. Wind fields analysis

A WRF-CFD model was used to analyze airflow and pollutant dispersion in this study. Figure 8a shows the time series of simulated and measured wind directions at AWS during the experiment period. Simulated wind directions in WRF-Chem and WRF-CFD simulations were similar to measured. However both models did not represent sudden changes of wind directions same as measured. The RMSEs of wind directions in WRF-Chem and WRF-CFD simulations are 91.58° and 88.17° , respectively (Table 2). The RMSEs of both model are not significant difference. Figure 8b shows the time series of simulated and measured wind speeds at AWS during experiment period. The wind speeds in WRF-Chem simulations were overestimated because WRF-Chem simulations do not reflect change of wind speeds by buildings that cause change of airflow in urban areas. On the other hand, the wind speeds in WRF-CFD simulations are similar to measured. RMSEs of wind speeds in WRF-Chem and WRF-CFD simulations are 3.15 m s^{-1} and 0.93 m s^{-1} , respectively

(Table 2). The RMSE of WRF-Chem simulations is larger than WRF-CFD because of overestimation in WRF-Chem simulations.

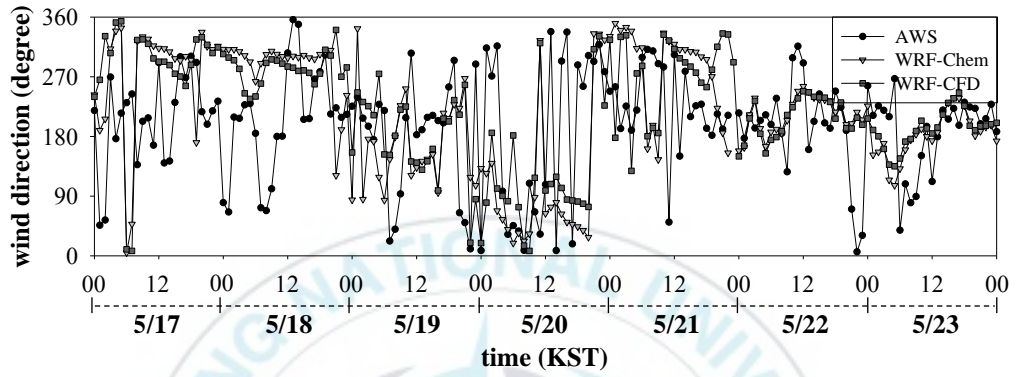
The wind directions and speeds of inflow are mostly changed by buildings in WRF-CFD simulations. If the building density is high in the direction entering inflow, change rates of wind direction and speed are high. Particularly change rate of wind speeds (hereafter deceleration rate) in WRF-CFD simulations are closely related with wind directions of inflow because the deceleration effect of wind speed by buildings is high. The wind directions of inflow were classified into four wind directions (east, west, south, and north) to analyze the deceleration rate in WRF-CFD simulations. The deceleration rate was calculated in Eq. (2).

$$R = \frac{SP_{WRF-Chem} - SP_{WRF-CFD}}{SP_{WRF-Chem}} \times 100$$

(2)

where, R means the deceleration rate in WRF-CFD simulations and $SP_{WRF-Chem}$ and $SP_{WRF-CFD}$ mean the wind speed in WRF-Chem and WRF-CFD simulations, respectively. The cases, that the simulated wind speed in WRF-CFD simulation was increased compared to inflow by low wind speed of inflow ($< 1 \text{ m s}^{-1}$), were excepted from analysis.

(a)



(b)

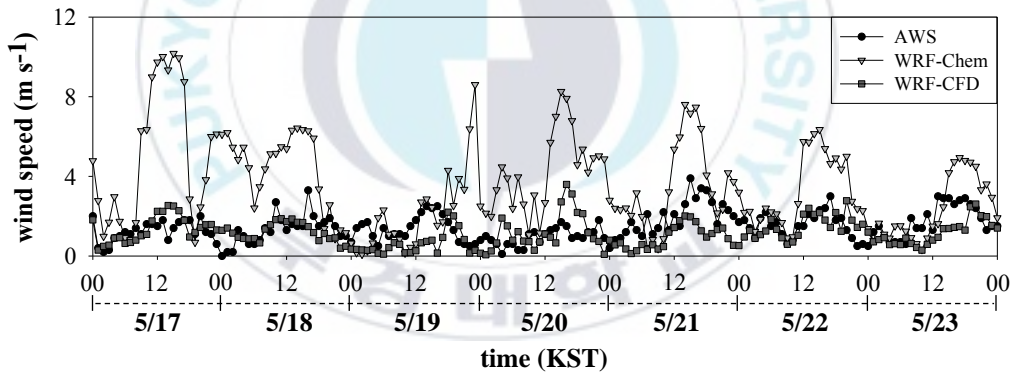


Fig. 8. (a) Time series of measured and simulated wind directions and (b) wind speeds at AWS. Black circles, grey triangles and dark grey squares represent measurements, WRF-Chem and WRF-CFD simulations, respectively.

Table 2. The root mean square errors (RMSEs) of simulated wind directions and speeds in WRF-Chem and WRF-CFD simulations.

RMSEs	wind direction (°)		wind speed (m s ⁻¹)	
	WRF-Chem	WRF-CFD	WRF-Chem	WRF-CFD
05.17	118.64	107.43	4.96	0.60
05.18	91.40	92.01	3.64	0.72
05.19	108.08	89.78	2.40	1.11
05.20	84.90	98.83	3.67	0.99
05.21	95.88	91.69	2.33	1.23
05.22	67.46	69.49	2.25	0.73
05.23	60.37	57.84	1.32	0.97
total	91.58	88.17	3.15	0.93

Figure 9 shows the degree of scattering for wind direction of inflow and the deceleration rate between WRF-Chem and WRF-CFD simulations at AWS. In cases that the wind direction of inflow is east (45 to 135°), the wind speed was decreased by more than 50% in 20 of 25 cases (80.00%). In cases of west (225 to 315°), the wind speed was decreased by more than 50% in 53 of 60 cases (88.33%). In cases of north (0 to 45° and 315 to 360°), the wind speeds

was decreased by more than 50% in 24 of 31 cases (77.43%). In cases that the wind direction of inflow is south (135 to 225°), the wind speed was decreased by less than 50% in 38 of 53 cases (71.70%). The wind speed was decreased by more than 30% and less than 50% in 27 of 53 cases (50.94%). Many buildings are located around AWS. The building density and height of buildings are high in the east and north of AWS. The building density is low in west of AWS, but the building that has big size and height is located in about 250 m away from AWS. When wind directions of inflow is east, west or north, the deceleration rate is high by buildings located in the east, west or north of AWS, respectively. The wind speed at AWS was reduced by up to 98.22% compared to wind speed of inflow. When wind direction of inflow is south, the deceleration rate is low because the building density is low and big and high buildings are not located in the south of AWS. Wind fields for each wind direction of inflow were analyzed to understand detailed airflow changed by buildings.

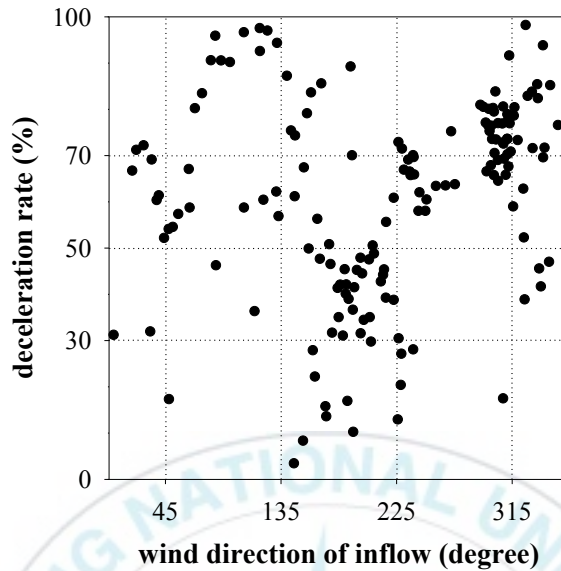


Fig. 9. The degree of scattering for wind direction of inflow and the deceleration rate between WRF-Chem and WRF-CFD simulations at AWS.

Figure 10a shows wind vectors and contours of vertical wind component for the object area at height of AWS ($z = 32.5$ m) in case that the wind direction of inflow is east (12 KST 20 May). A rectangle with red solid line and red circles represents region of Figure 10b and location of AWS, respectively. The wind direction and speed of inflow are 63.82° and 2.68 m s^{-1} , respectively. Wind speeds in the whole domain are low by low wind speed of inflow. Airflow is similar to inflow in the river in the northeast of the domain because there are not buildings. Descending and divergence of airflow represent in the northwest of the domain by airflow entering the low-altitude river. The

simulated wind direction and speed at AWS are effected by high buildings located in east of AWS. Inflow entering from east of the domain are divergence toward the lower level and flank of the buildings by buildings (A) located in the east of AWS.

Airflow entering narrow canyon in the south of (A) diverge to wide area located in AWS. The wind speed of diverged airflow is lower than airflow entering narrow canyon by the channeling effect. Channeling effect refers to phenomenon that the speed of fluid are decreased (increased) by the law of the conservation of mass when fluid passes from a narrow (wide) place to a wide (narrow) place. In same principal, wind speed is decreased by channeling effect when airflow passes from narrow area in the south of (A) to wide area located in AWS. The simulated wind direction (98.46°) at AWS (red circle in Fig. 10b) differs from inflow by diverged airflow. The simulated wind speed (1.11 m s^{-1}) decreased 58.76% compared to inflow is similar to measured (1.10 m s^{-1}) at AWS.

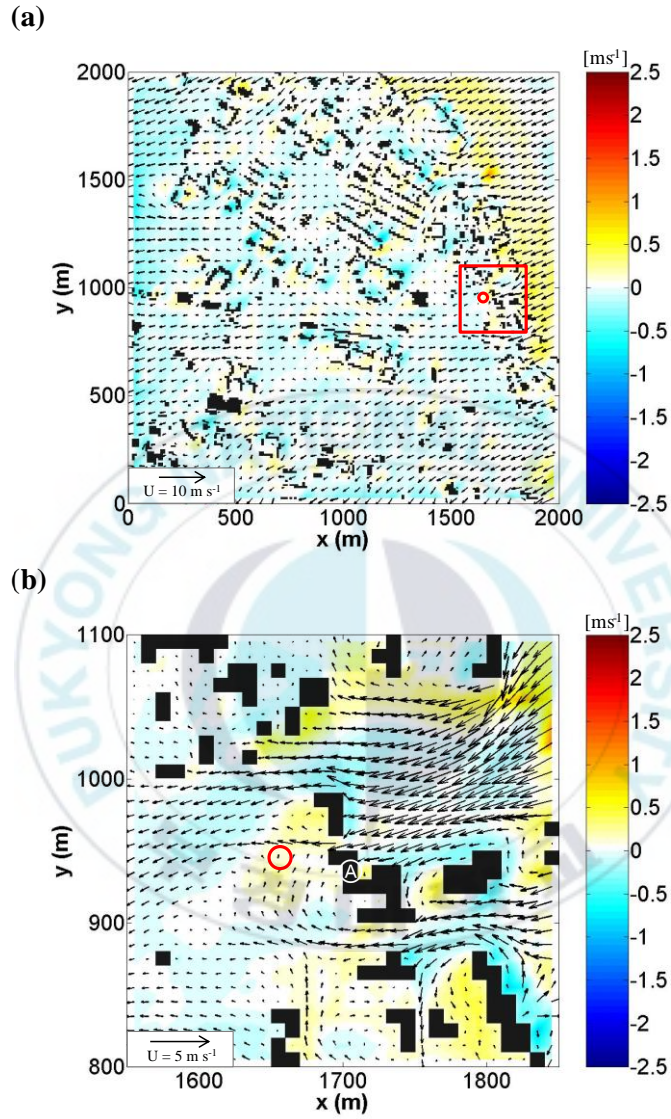


Fig. 10. Wind vectors ($\sqrt{U^2 + V^2}$) and contours of vertical wind (W) components at $z = 32.5$ m at 12 KST 20 May. A rectangle with red solid line represents region of (b) and red circles represent location of AWS.

Figure 11a shows wind vectors and contours of vertical wind component in case that the wind direction of inflow is west (17 KST 17 May). A rectangle with red solid line and red circles represents region of Figure 11b and location of AWS, respectively. The wind direction and speed of inflow are 300.78° and 8.76 m s^{-1} , respectively. Wind speeds in the whole domain are high by high wind speed of inflow. Airflow is similar to inflow in the river. Wind directions change from the west-northwest to west when inflow enters street canyon in center of the domain (a rectangle with red dash line in Fig. 11a). The change of wind directions affect the surrounding of AWS. The westerly wind is diverged by building (㉔) located in the west of AWS (Fig. 11b). When airflow hits the building, a stagnation point is formed and airflow is diverged according to the stagnation point. Ascending and descending airflow occur in up and down direction of the stagnation point, respectively. The diverged airflow to flank of the building enters toward downwind area along building. The airflow is converged to a point in the downwind area of the building, called reattachment point and recirculation region is formed in this area. The circulation of two eddies appear, called double-eddy circulation in cross-section of the recirculation region. As has been previously explained, the double-eddy circulation appears in recirculation region of the ㉔. Westerly wind is changed to west-southwesterly wind by double-eddy circulation. The

simulated wind direction (256.2°) at AWS (red circle in Fig. 11b) differs from inflow. The simulated wind speed (1.79 m s^{-1}) decreased 79.50% compared to inflow is similar to measured wind speed (1.80 m s^{-1}) at AWS.

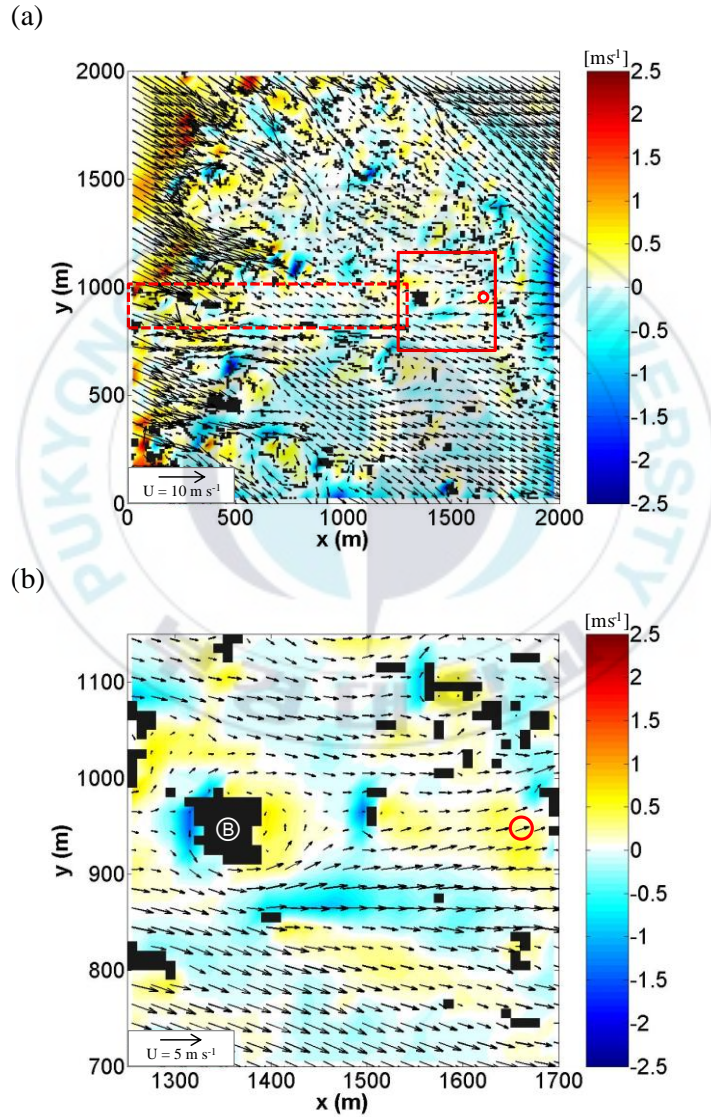


Fig. 11. The same as in Figure 10 except for the 17 KST 17 May case.

Figure 12a shows wind vectors and contours of vertical wind component in case that the wind direction of inflow is north (21 KST 20 May). A rectangle with red solid line and red circles represents region of Figure 12b and location of AWS, respectively. The wind direction and speed of inflow are 334.97° and 4.93 m s^{-1} , respectively. The wind speed of inflow is high, but the simulated wind speeds in the whole domain are low overall because the building density is high in the north of the domain entering inflow. Many high buildings are located in the north of AWS. Inflow is changed by buildings located in the north of AWS and the changed airflow enters to AWS. Airflow entering from the north is diverged by building (©) and wind directions and speeds of airflow are changed (Fig. 12b). Wind speeds are decreased and wind direction are changed from the north to northwest. The diverged airflow enters almost intactly to AWS because factors that affect to change of airflow are not exist between © and AWS. The simulated wind direction (311.45°) at AWS differs from inflow. The simulated wind speed (1.79 m s^{-1}) is decreased 79.50% compared inflow at AWS. The simulated wind speed is underestimated compared measured wind speed.

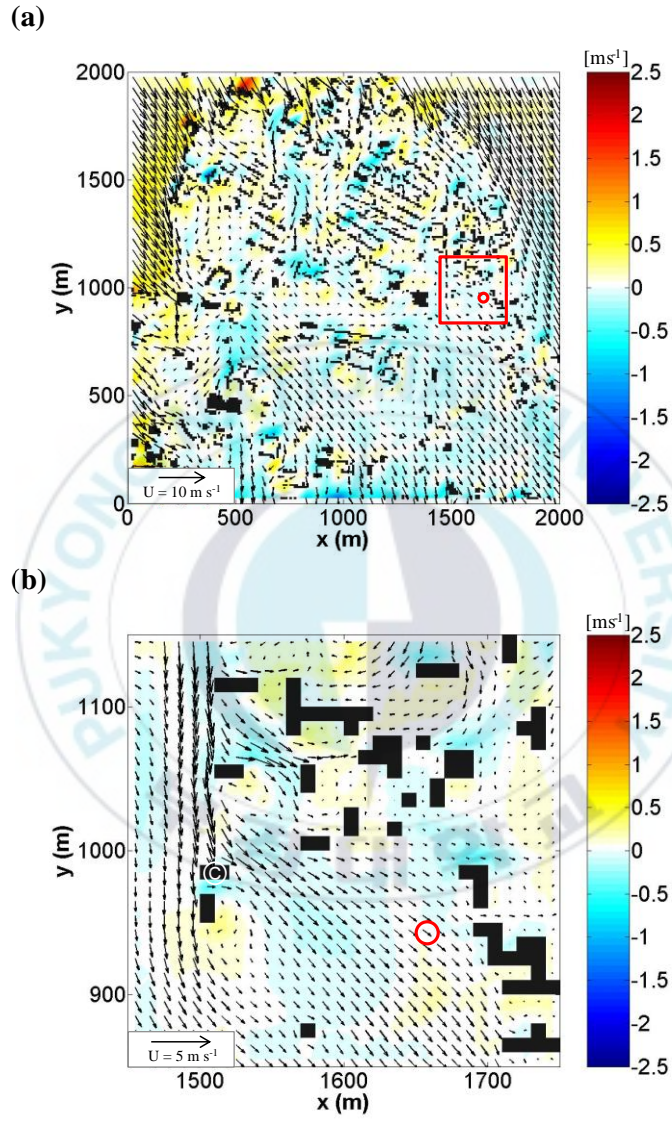


Fig. 12. The same as in Figure 10 except for the 21 KST 20 May case.

Figure 13a shows wind vectors and contours of vertical wind component in case of northerly (21 KST 23 May). A rectangle with red solid line and red circles represents region of Figure 13b and location of AWS, respectively. The wind direction and speed of inflow are 187.64° and 3.32 m s^{-1} , respectively. The wind direction of inflow is maintained because the building density in the south of the domain is low. The wind speeds are slightly decreased by surface friction and so on. Airflow similar to inflow enters to AWS because the big or high buildings that affect to change of airflow are not exist in the south of AWS. The change effect of wind direction and deceleration effect are small by the low building density in the south of AWS. The simulated wind direction (195.42°) at AWS (red circle in Fig. 13b) is similar to inflow (187.63°). The simulated wind speed (2.03 m s^{-1}) decreased 39.00% compared inflow is similar to measured (1.90 m s^{-1}) at AWS.

The CFD model simulates well change of airflow by building effect such as deceleration of wind speed, divergence of airflow, eddy circulation, channeling effect and so on. In the next verse, the concentration fields were analyzed to understand pollutant dispersion by airflow on the basis of wind fields simulated from CFD model.

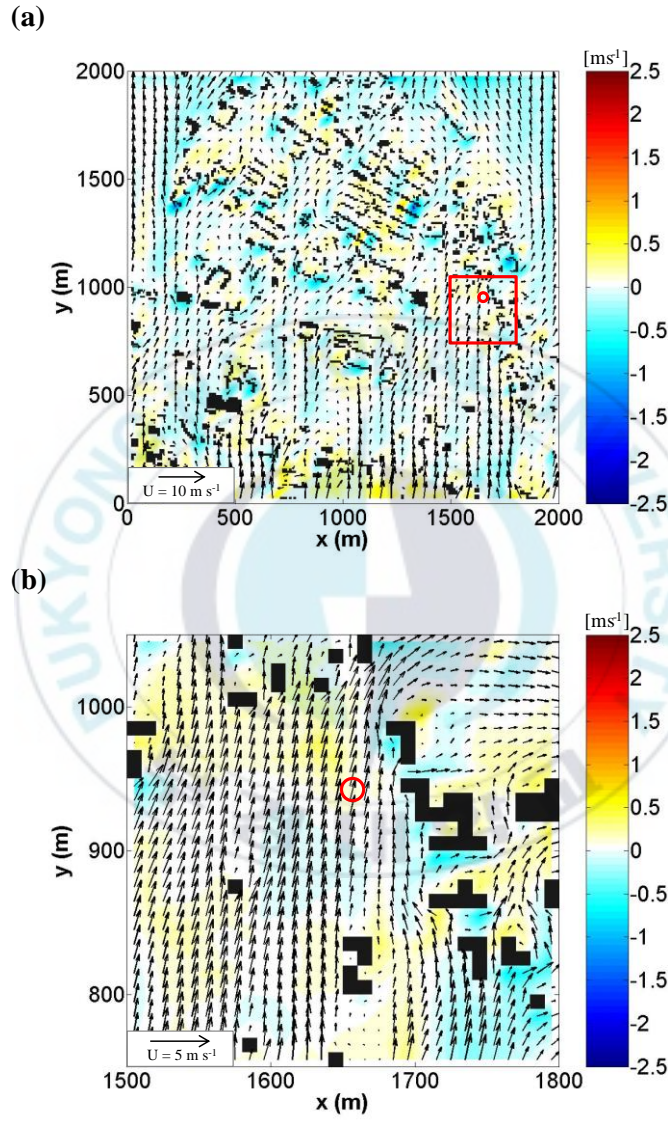


Fig. 13. The same as in Figure 10 except for the 21 KST 23 May case.

3.2. Concentration fields analysis

The simulated CO concentrations in WRF-Chem and WRF-CFD simulations are analyzed to understand pollutant dispersion by airflow. Figure 14a shows the time series of the simulated and measured CO concentrations at AQMS during the experiment period. The CO emissions are high during the daytime. However CO concentrations are low by high wind speeds of inflow. The RMSEs of CO concentrations in WRF-Chem and WRF-CFD simulations are 0.43 ppm and 0.30 ppm, respectively (Table 3). The RMSE in WRF-CFD simulations is lower than in WRF-Chem simulations. The simulated CO concentrations in WRF-Chem simulations are underestimated compared with measured CO concentrations. The simulated wind speeds ($\sqrt{U^2 + V^2} < 10.20 \text{ m s}^{-1}$) in WRF-Chem simulations are higher than the absolute values of vertical wind components ($|W| < 0.05 \text{ m s}^{-1}$) (Fig. 14b and 14c). The horizontal CO dispersion is occurred more actively than the vertical. Then surface CO cannot be dispersed well to height of AQMS (Fig. 15). Therefore, simulated CO concentrations in WRF-Chem simulations are not significantly affected by the CO emissions and are similar to background CO concentrations at AQMS. The absolute values of vertical wind components in WRF-CFD simulations are

higher than WRF-Chem simulations because of building effect. Therefore, the diurnal variations of CO concentrations are appeared in WRF-CFD simulations following the CO emissions. When the CO emissions are low ($< 0.5 \times 10^{-5} \text{ kg m}^{-2} \text{ s}^{-1}$), CO concentration is low ($< 0.5 \text{ ppm}$) (00 KST to 05 KST). When the CO emissions are high ($> 1.2 \times 10^{-5} \text{ kg m}^{-2} \text{ s}^{-1}$), CO concentration is high ($> 0.6 \text{ ppm}$) (07 KST to 08 KST).

Table 3. The root mean square errors (RMSEs) of simulated CO concentrations in WRF-Chem and WRF-CFD simulations.

RMSEs	CO concentration (ppm)	
	WRF-Chem	WRF-CFD
05.17	0.57	0.36
05.18	0.51	0.31
05.19	0.38	0.38
05.20	0.37	0.26
05.21	0.23	0.24
05.22	0.38	0.24
05.23	0.49	0.30
total	0.43	0.30

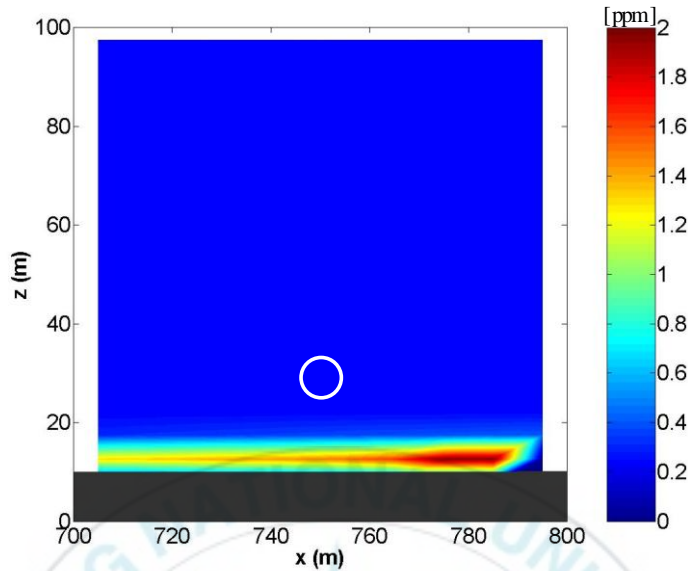


Fig. 15. The contours of CO concentration in a vertical plane around AQMS. White circle represent AQMS.

Figure 16a shows the degree of scattering between the simulated CO concentrations in WRF-CFD and CO emissions. The higher CO emission is, the higher the CO concentration is. CO emission are high, but the CO concentrations are low in some cases (rectangle in Fig. 16a). Figure 16b shows the degree of scattering between the simulated CO concentrations in WRF-CFD and time. This shows the change of the CO concentrations over time. The CO concentration is high by high CO emission at commuting time (07 to 08 KST/ 18 to 20 KST). The CO concentration is low despite high CO emission at daytime (10 to 16 KST) because of high wind speed. The CO concentration

is low at nighttime (00 to 05 KST/ 22 to 24 KST) by low CO emission because traffic volume is low. The wind and concentration fields were analyzed by dividing commuting time, daytime and nighttime to analyze the difference of CO concentrations over time.

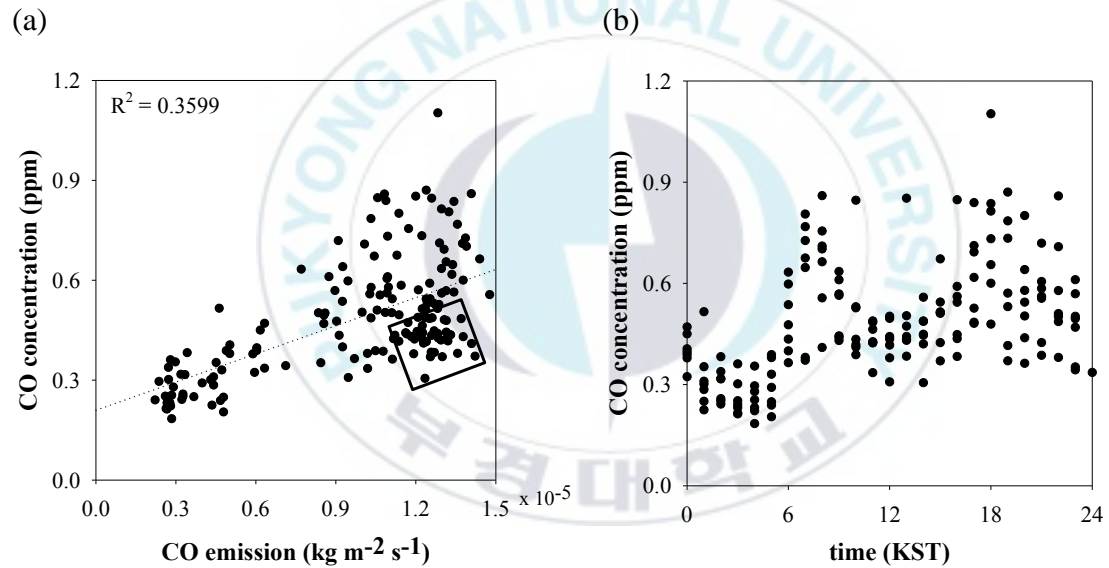


Fig. 16. (a) The degree of scattering between the simulated CO concentrations in WRF-CFD and CO emissions and (b) time.

Figure 17 shows wind vectors and contours of vertical wind components (Fig. 17a and 17c) and contours of CO concentrations (Fig. 17b and 17d) in the object area at height of AQMS ($z = 27.5$ m) at 18 KST 22 May. Rectangles with red solid line and red circles represent region of Figure 17c and 17d and location of AQMS, respectively. The wind direction and speed of inflow and CO emission are 216.78° , 4.89 m s^{-1} and $1.28 \times 10^{-5} \text{ kg m}^{-2} \text{ s}^{-1}$, respectively. The CO concentration are high overall by high CO emission at commuting time. CO is dispersed to northeast by inflow (southwesterly). The CO concentrations are high along the roads emitted CO. And the CO concentrations are high at downwind area of building. In horizontal case, CO is entered to downwind area by double-eddy circulation formed at downwind area. CO is not actively dispersed because the wind speeds are low at downwind area. Therefore, the CO concentrations are high at downwind areas. In vertical case, vertical eddy circulation is formed at downwind area of building (Fig. 18). The CO concentrations are high at downwind areas because ascending CO is not well escaped to outside by eddy circulation. The CO concentrations are high in the southwest of AQMS. The CO emitted from roads and the CO entered from the south by southerly are entered to AQMS by southwesterly. Some of the CO are entered to downwind area of buildings located in the southwest by horizontal double-eddy circulation. The simulated

CO concentration (1.10 ppm) at AQMS is higher than measured (0.40 ppm) by CO entered to AQMS. However, the CO concentration at AQMS is lower than around because the CO is dispersed by descending airflow at AQMS located of upwind area of building (D).

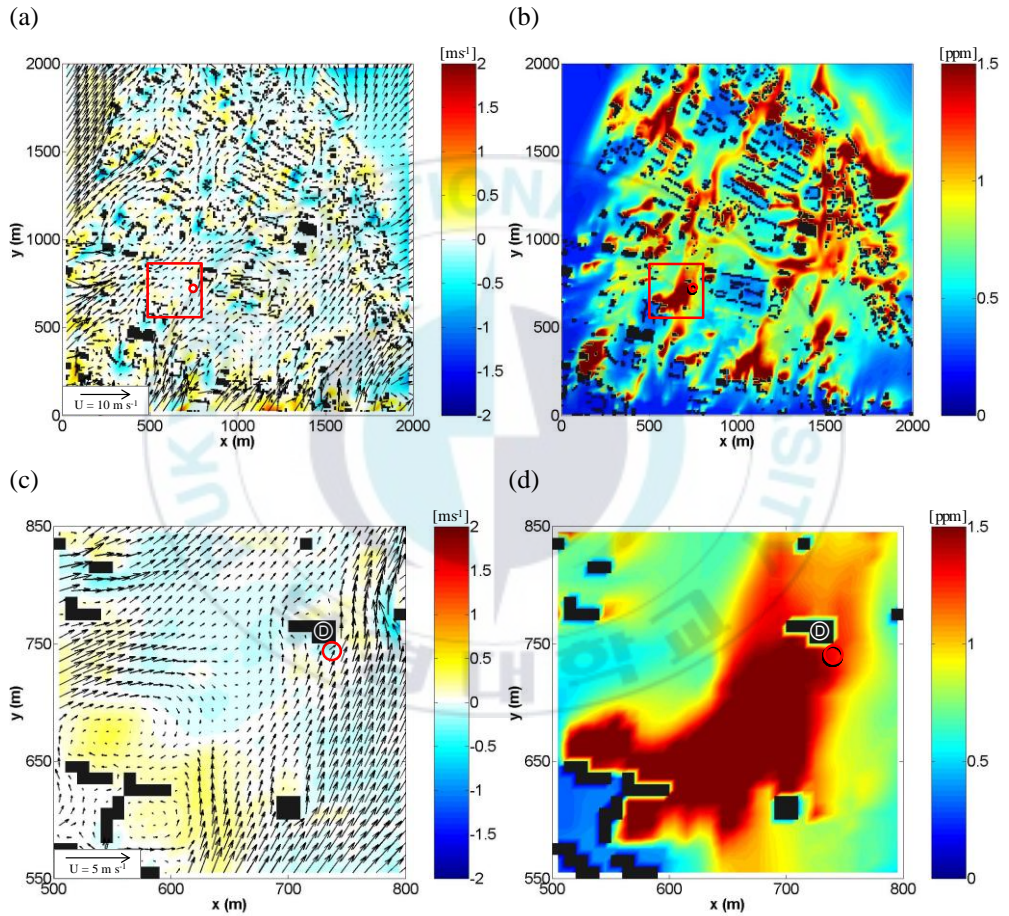


Fig. 17. (left panels) Wind vectors ($\sqrt{U^2 + V^2}$) and contours of vertical wind (W) components and (right panels) contours of CO concentration at $z = 27.5$ m at 18 KST 22 May. Red rectangles represent region of (c) and (d) and red circles represent location of AQMS.

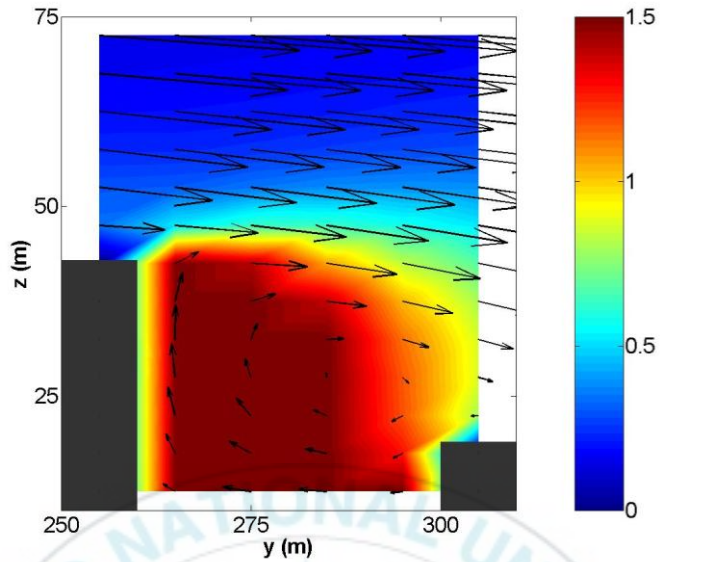


Fig. 18. The wind vector and contours of CO concentration in a vertical plane at street canyon.

Figure 19 shows wind vectors and contours of vertical wind components (Fig. 19a and 19c) and contours of CO concentrations (Fig. 19b and 19d) at 15 KST 22 May. The wind direction and speed of inflow and CO emission are 235.82° , 6.25 m s^{-1} and $1.22 \times 10^{-5} \text{ kg m}^{-2} \text{ s}^{-1}$, respectively. The wind direction of inflow and CO emission are similar to previous case, but the wind speed of inflow differs from previous case. The CO concentrations are lower than previous case overall because the wind speed of inflow is high at daytime. The CO concentrations are high at downwind area of building by horizontal or vertical eddy circulations. The CO concentrations are low because CO is well dispersed by high wind speed of southwesterly at the west of AQMS. The CO

concentrations are high at downwind areas of buildings located in the southwest because CO is entered to downwind areas by strong horizontal double-eddy circulation. Some of the CO are entered to AQMS. The CO concentration at AQMS is higher than around. The CO concentrations are low at the south of AQMS by high wind speed and descending airflow. The simulated CO concentration (0.51ppm) is similar to measured CO concentration (0.50 ppm) at AQMS by high wind speed despite high CO emission.

Figure 20 shows wind vectors and contours of vertical wind components (Fig. 20a and 20c) and contours of CO concentrations (Fig. 20b and 20d) at 04 KST 22 May. The wind direction and speed of inflow and CO emission are 206.54° , 2.27 m s^{-1} and $0.28 \times 10^{-5} \text{ kg m}^{-2} \text{ s}^{-1}$, respectively. The wind direction is similar to previous cases, but the wind speed of inflow and CO emission are very low. The CO concentrations are low overall by low CO emission at nighttime. The CO concentrations are high mainly along the roads emitted CO because CO is not actively dispersed by low wind speed of inflow. In previous cases, the big double-eddy circulations were formed in downwind areas of buildings located in the southwest of AQMS. However, in this case, the small double-eddy circulations are formed by low wind speed of inflow. The areas accumulated CO are small by small double-eddy circulations. The CO

concentration at AQMS is mainly affected by airflow (southerly) entering from the south. The CO concentration entered to AQMS is low because of high wind speeds and descending airflow. AQMS is located in upwind area of ㉔ where descending airflow is formed. The simulated CO concentration (0.23 ppm) at AQMS is lower than measured CO concentration (0.60 ppm) by low CO emission and high wind speeds and descending flows around AQMS.

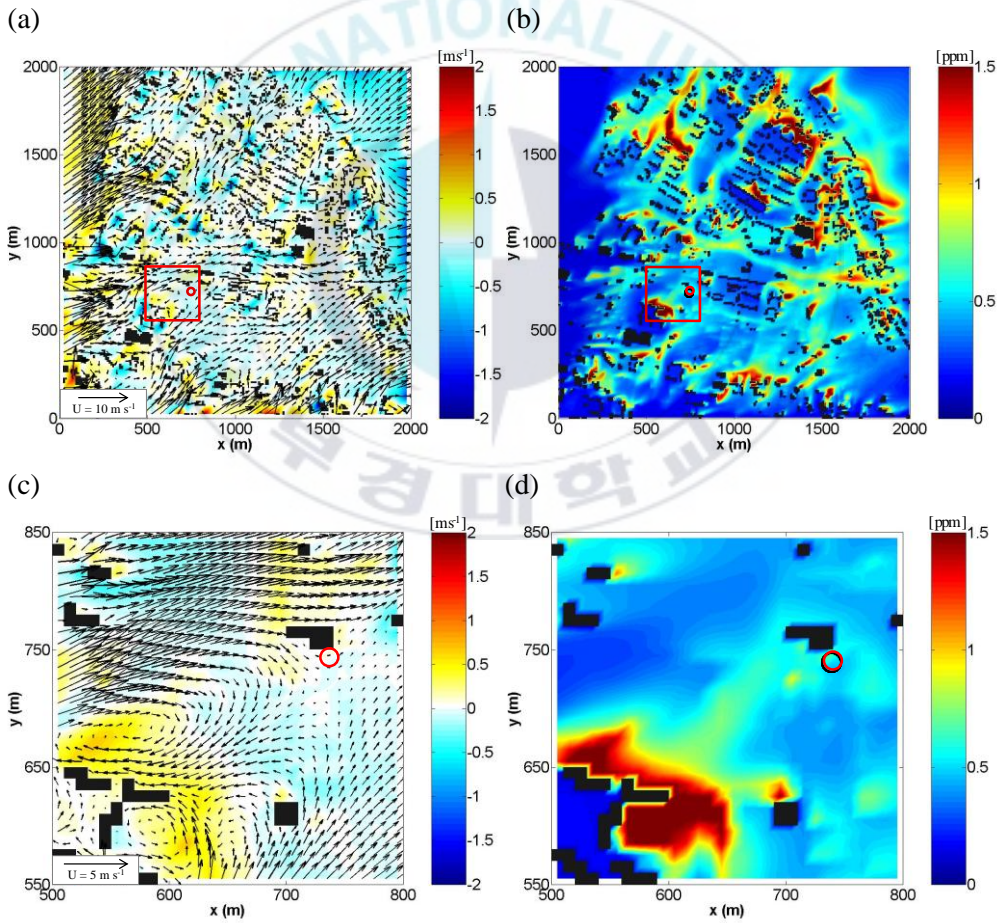


Fig. 19. The same as in Figure 15 except for the 15 KST 22 May case.

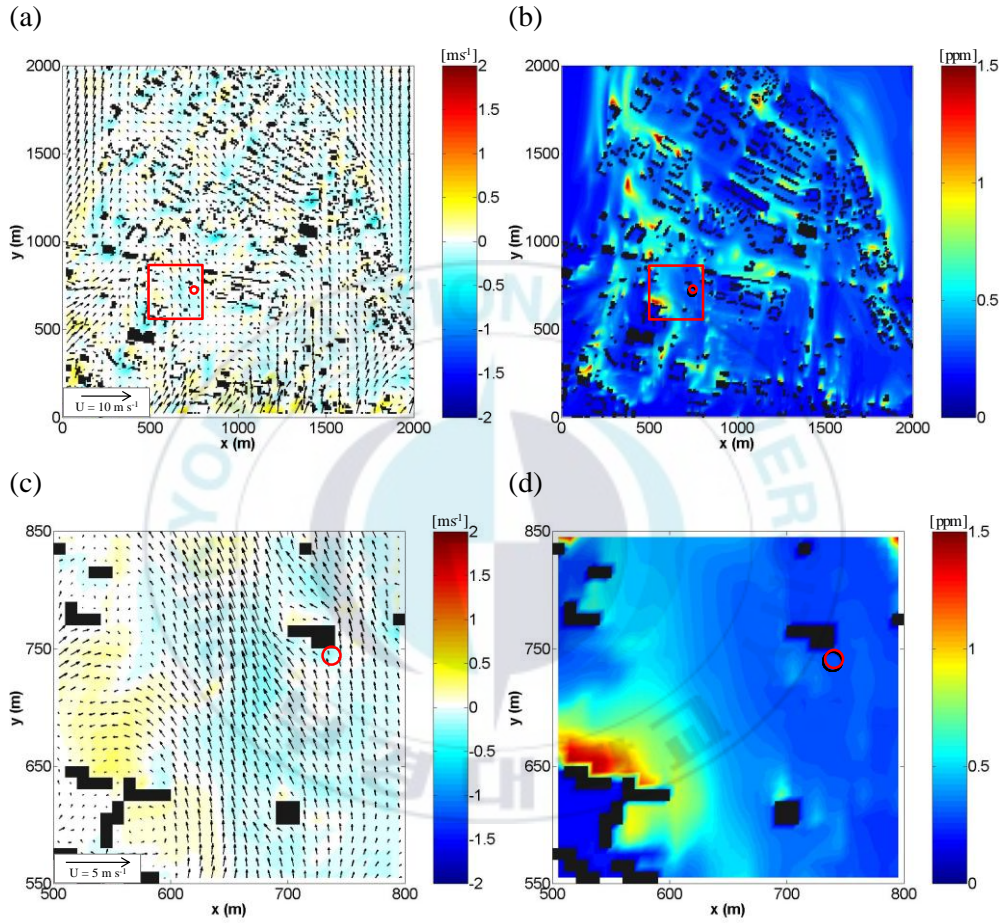


Fig. 20. The same as in Figure 15 except for the 04 KST 22 May case.

4. Summary and Conclusion

In this study, airflow and non-reactive pollutant (CO) dispersion were analyzed using CFD model coupled with WRF-Chem model (WRF-CFD model) in an urban area. Yeongdeungpo-gu, Seoul, Korea was selected as the object area for the simulations. WRF-Chem simulations were performed to use the simulated data as the background fields in WRF-CFD model. The anthropogenic data in SMOKE-Asia (Woo et al., 2012) was used as the CO emissions in WRF-Chem model. Numerical experiments were performed using simulated wind data and CO concentrations as inflow boundary data in WRF-CFD model.

As a result, the simulated wind directions in WRF-Chem and WRF-CFD simulations were similar to measured wind direction. However both models did not represent sudden changes of wind directions same as measured. The RMSEs of the wind directions in WRF-Chem (91.58°) and WRF-CFD simulations (88.17°) were similar. The RMSE of both model is not significant difference. The simulated wind speeds in WRF-Chem simulations were overestimated because WRF-Chem model did not consider detailed

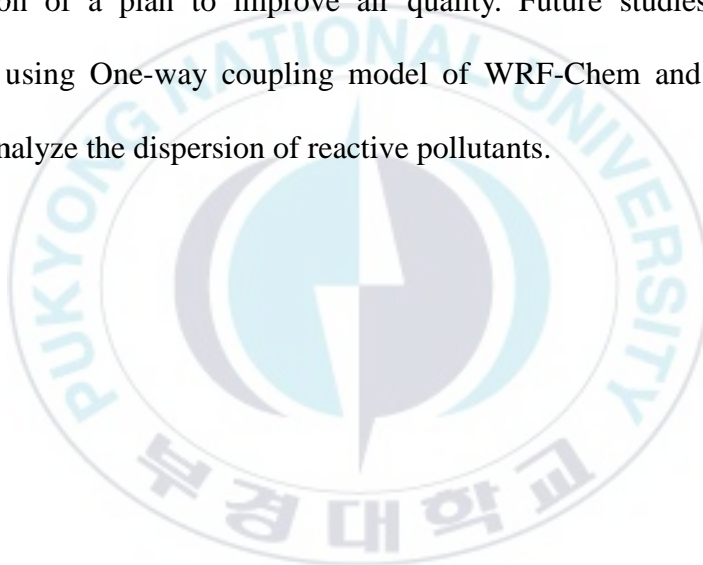
topography and buildings information. On the other hand, the simulated wind speeds in WRF-CFD simulations that considered detailed topography and buildings information were similar to measured wind speeds. The RMSEs of the wind speeds in WRF-CFD simulations (0.93 m s^{-1}) were lower than WRF-Chem simulations (3.15 m s^{-1}). The deceleration rate of simulated wind speed in WRF-CFD compared to inflow were different depending on the wind direction of inflow. The wind directions of inflow were classified into east, west, south and north for analysis of deceleration rates. In case that wind direction of inflow was east, west or north, the deceleration rate was high because the buildings affecting airflow were located in the east, west or north of AWS, respectively. In case of south, the deceleration rate was low because the buildings affecting airflow were not located in the south of AWS. The CFD model simulated well change of airflow by buildings. The concentration fields were analyzed to understand pollutant dispersion by airflow on the basis of wind fields simulated from CFD model.

To simulate of CO dispersion, the timely CO emissions were calculated using the daily CO emissions in the object area. The simulations of CO dispersion were perform using calculated CO emissions and simulated wind data in WRF-Chem and WRF-CFD simulations. The simulated CO concentrations in WRF-Chem were used as background CO. The simulated

CO concentrations in the simulations using simulated wind data in WRF-Chem were underestimated for measured at AQMS. The horizontal wind speeds ($\sqrt{U^2 + V^2} < 10.20 \text{ m s}^{-1}$) were higher than the absolute values of vertical wind components ($|W| < 0.05 \text{ m s}^{-1}$) at AQMS. The horizontal dispersion of CO was more active than vertical. The simulated CO concentrations at AQMS were low because surface CO was not diffused to AQMS. The simulated CO concentrations in WRF-CFD simulations were similar to measured CO concentrations with the exception of 00 KST to 05 KST when the CO emissions were low ($< 0.5 \times 10^{-5} \text{ kg m}^{-2} \text{ s}^{-1}$) because of low traffic at the time. The RMSE of the wind directions in WRF-CFD simulations (0.30 ppm) was lower than WRF-Chem simulations (0.43 ppm). The CO concentration was mainly affected by CO emission. The simulated CO concentrations was high at commuting time that CO emission was high. The simulated CO concentration was low at nighttime that CO emission was low by low traffic. The CO emission was high at daytime, but the simulated CO concentration was low by high wind speeds.

Airflow and pollutants dispersion are very important factor to be considered in urban areas where many emission sources exist and airflow is constantly changing because of buildings. Through this study, it is concluded and confirmed that one-way coupling model of WRF-Chem and WRF-CFD

model is useful to analyze airflow and pollutants dispersion. As the results of this study suggest, it is possible to identify high concentration areas, because of the accumulation of pollutants, using the analysis of airflow and pollutants dispersion. The conclusion of this study suggests that the suitable point of the area to monitor air quality that represents the general air quality of the area and the air quality of high concentration area. Furthermore, this study may lead to a suggestion of a plan to improve air quality. Future studies should be conducted using One-way coupling model of WRF-Chem and WRF-CFD model to analyze the dispersion of reactive pollutants.



REFERENCES

- Ai, Z. T. and C. M. Mark, 2013: CFD simulation of flow and dispersion around an isolated building: Effect of inhomogeneous ABL and near-wall treatment. *Atmospheric Environment*, **77**, 568-578.
- Amirjamshidi, G., T. S. Mostafa, A. Misra, and M. J. Roorda, 2013: Integrated model for microsimulating vehicle emissions, pollutant dispersion and population exposure. *Transportation Research Part D: Transport and Environment*, **18**, 16-24.
- Baik, J. J., K. H. Kwak, S. B. Park, and Y. H. Ryu, 2012: Effects of building roof greening on air quality in street canyons. *Atmospheric Environment*, **61**, 48-55.
- Baldauf, R. W., D. Heist, V. Isakov, S. Perry, G. S. W. Hagler, S. Kimbrough, R. Shores, and L. Brixey, 2013: Air quality variability near a highway in a complex urban environment. *Atmospheric Environment*, **64**, 169-178.
- Barnard, J. C., E. G. Chapman, J. D. Fast, J. R. Schemlzer, J. R. Slusser, and R. E. Shetter, 2004: An evaluation of the FAST-J photolysis algorithm for predicting nitrogen dioxide photolysis rates under clear and cloudy sky conditions, *Atmospheric Environment*, **38**, 3393-3403.

Bohnenstengel, S. I., S. E. Belcher, A. Aiken, J. D. Allan, G. Allen, A. Bacak, T. J. Bannan, J. F. Barlow, D. C. S. Beddows, W. J. Bloss, A. M. Booth, C. Chemel, O. Coceal, C. F. Di Marco, M. K. Dubey, K. H. Faloon, Z. L. Fleming, M. Furger, J. K. Gietl, R. R. Graves, D. C. Green, C. S. B. Grimmond, C. H. Halios, J. F. Hamilton, R. M. Harrison, M. R. Heal, D. E. Heard, C. Helfter, S. C. Herndon, R. E. Holmes, J. R. Hopkins, A. M. Jones, F. J. Kelly, S. Kotthaus, B. Langford, J. D. Lee, R. J. Leigh, A. C. Lewis, R. T. Lidster, F. D. Lopez-Hilfiker, J. B. McQuaid, C. Mohr, P. S. Monks, E. Nemitz, N. L. Ng, C. J. Percival, A. S. H. Prévôt, H. M. A. Ricketts, R. Sokhi, D. Stone, J. A. Thornton, A. H. Tremper, A. C. Valach, S. Visser, L. K. Whalley, L. R. Williams, L. Xu, D. E. Young, and P. Zotter, 2015: Meteorology, Air Quality, and Health in London: The ClearfLo Project. *Bulletin of the American Meteorological Society*, **96**, 779–804.

City of Los Angeles, 2013: City of Los Angeles 2010 Bicycle Plan: First Year of the First Five-Year Implementation Strategy and Figueroa Streetscape Project – 4.1 Air Quality. *City of Los Angeles*, 1.

Clapp, L. J., and M. E. Jenkin, 2001: Analysis of the relationship between ambient levels of O₃, NO₂ and NO as a function of NO_x in the UK. *Atmospheric Environment*, **35-36**, 6391-6405.

Fuglestvedt, J. S., Isaksen, I. S., Wang, W. C., 1996: Estimates of indirect global

warming potentials for CH₄, CO and NO_x. *Climatic Change*, **34-3**, 405–437.

Gousseau, P., B. Blocken, T. Stathopoulos, and G. J. F. Van, 2011: CFD simulation of near-field pollutant dispersion on a high-resolution grid: a case study by LES and RANS for a building group in downtown Montreal. *Atmospheric Environment*, **45-2**, 428-438.

Habilomatis, G., and A. Chaloulakou, 2015: A CFD modeling study in an urban street canyon for ultrafine particles and population exposure: The intake fraction approach. *Science of the Total Environment*, **530**, 227-232.

Janjic, Z. I., 1990: The step-mountain coordinate: physical package. *Monthly Weather Review*, **118-7**, 1429–1443.

_____, 1994: The step-mountain eta coordinate model: further developments of the convection, viscous sublayer, and turbulence closure schemes. *Monthly Weather Review*, **122-5**, 927–945.

Jenkin, M. E., 2004: Analysis of sources and partitioning of oxidant in the UK—Part 2: contributions of nitrogen dioxide emissions and background ozone at a kerbside location in London. *Atmospheric Environment*, **38-30**, 5131-5138.

Kwak, K. H., and J. J. Baik, 2012: A CFD modeling study of the impacts of NO_x and VOC emissions on reactive pollutant dispersion in and above a street canyon. *Atmospheric Environment*, **46**, 71-80.

- _____, J. J. Baik, Y. H. Ryu, and S. H. Lee, 2015: Urban air quality simulation in a high-rise building area using a CFD model coupled with mesoscale meteorological and chemistry-transport models. *Atmospheric Environment*, **100**, 167-177.
- Kim, J. J., E. Pardyjak, D. Y. Kim, K. S. Han, and B. H. Kwon, 2014: Effects of Building-Roof Cooling on Flow and Air Temperature in Urban Street Canyons. *Asia-Pacific Journal of Atmospheric Sciences*, **50-3**, 365-375.
- Kim, M. J., R. J. Park, and J. J. Kim, 2012: Urban air quality modeling with full O₃–NO_x–VOC chemistry: Implications for O₃ and PM air quality in a street canyon. *Atmospheric Environment*, **47**, 330-340.
- Kwon, A. R., and J. J. Kim, 2014: Study on Detailed Air Flows in Urban Areas Using GIS Data in a Vector Format and a CFD Model. *Korean Journal of Remote Sensing*, **30-6**, 755-767 (In Korean).
- _____, and J. J. Kim, 2015: Analysis on the Observation Environment of Surface Wind Using GIS data. *Korean Journal of Remote Sensing*, **31-2**, 65-75 (In Korean).
- Li, Q., C. Chen, Y. Deng, J. Li, G. Xie, Y. Li, and Q. Hu, 2015: Influence of traffic force on pollutant dispersion of CO, NO and particle matter (PM 2.5)

measured in an urban tunnel in Changsha, China. *Tunnelling and Underground Space Technology*, **49**, 400-407.

Life Science Dictionary Compilation Committee, 2003: *Life Science Dictionary*. Academy Seojeok, 139 (In Korean).

Maeng, Y. S. and T. R. Heo, 2002: *Food and Health*. Yuhan Munhwasa, 349-350 (In Korean).

Masiol, M., A. Hofer, S. Squizzato, R. Piazza, G. Rampazzo, and B. Pavoni, 2012: Carcinogenic and mutagenic risk associated to airborne particle-phase polycyclic aromatic hydrocarbons: a source apportionment. *Atmospheric Environment*, **60**, 375-382.

Miao, Y., S. Liu, B. Chen, B. Zhang, S. Wang, and S. Li, 2013: Simulating urban flow and dispersion in Beijing by coupling a CFD model with the WRF model. *Advances in atmospheric sciences*, **30**, 1663-1678.

Montazeri, H., B. Blocken, D. Derome, J. Carmeliet, and J. L. M. Hensen, 2015: CFD analysis of forced convective heat transfer coefficients at windward building facades: influence of building geometry. *Journal of Wind Engineering and Industrial Aerodynamics*, **146**, 102-116.

- Park, R. J., S. K. Hong, H. A. Kwon, S. Kim, A. Guenther, J. H. Woo, and C. P. Loughner, 2014: An evaluation of ozone dry deposition simulations in East Asia. *Atmospheric Chemistry and Physics*, **14-15**, 7929-7940.
- Rakowska, A., K. C. Wong, T. Townsend, K. L. Chan, D. Westerdahl, S. Ng, G. Močnik, L. Drinovec, and Z. Nin, 2014: Impact of traffic volume and composition on the air quality and pedestrian exposure in urban street canyon. *Atmospheric Environment*, **98**, 260-270.
- Rissler, J., E. Swietlicki, A. Bengtsson, C. Boman, J. Pagels, T. Sandström, A. Blomberg, and J. Löndahl, 2012: Experimental determination of deposition of diesel exhaust particles in the human respiratory tract. *Journal of aerosol science*, **48**, 18-33.
- Tominaga, Y., and T. Stathopoulos, 2011: CFD modeling of pollution dispersion in a street canyon: Comparison between LES and RANS. *Journal of Wind Engineering and Industrial Aerodynamics*, **99-4**, 340-348.
- Versteeg, H. K., and W. Malalasekera, 1995. *An Introduction to Computational Fluid Dynamics : The Finite Volume Method*, Longman, Malaysia, 257.
- Wild, O., X. Zhu, and M. J. Prather, 2000: Fast-J: Accurate Simulation of In- and Below-Cloud Photolysis in Tropospheric Chemical Models. *Journal of Atmospheric Chemistry*, **37**, 245–282.

World Health Organization, 2008: Air quality and health - Fact sheet No. 313.

Geneva: World Health Organization,

<http://www.who.int/mediacentre/factsheets/fs313/en/>.

Yakhot, V., S. A. Orszag, S. Thangam, T. B. Gatski, and C. G. Speziale, 1992:

Development of turbulence models for shear flows by a double expansion technique. *Physics of Fluids*, **4**, 1510-1520.

Zavala, M., S. C. Herndon, R. S. Slott, E. J. Dunlea, L. C. Marr, J. H. Shorter, and M.

J. Molina, 2006: Characterization of on-road vehicle emissions in the Mexico City Metropolitan Area using a mobile laboratory in chase and fleet average measurement modes during the MCMA-2003 field campaign. *Atmospheric Chemistry and Physics*, **6-12**, 5129-5142.

Zaveri, R. A., and L. K. Peters, 1999: A new lumped structure photochemical

mechanism for largescale applications. *Journal of Geophysical Research: Atmospheres (1984–2012)*, **104-D23**, 30387-30415.

Zhang, H., and Q. Ying, 2011: Contributions of local and regional sources of NO_x to

ozone concentrations in Southeast Texas. *Atmospheric Environment*, **45-17**, 2877-2887.

Zheng, Y., Y. Miao, S. Liu, B. Chen, H. Zheng, and S. Wang, 2015: Simulating Flow and Dispersion by Using WRF-CFD Coupled Model in a Built-Up Area of Shenyang, China. *Advances in Meteorology*, **2015**.



감사의 말

어느새 석사과정을 마치고 학위 논문을 제출하게 되었습니다. 지난 2 년 의 시간 동안 저에게 도움을 주신 분들이 많습니다. 미흡하지만 학위 논문을 마치면서 그 분들께 감사의 말씀을 전합니다. 누구보다도 많은 도움을 주시고, 부족한 점을 언제나 세심하고 꼼꼼한 손길로 지적해주신 김재진 교수님께 진심으로 감사 드립니다. 또한 같이 짧은 기간 동안 많은 격려와 조언을 해주신 최원식 박사님께도 감사 드립니다. 바쁘신 중에도 논문 심사를 맡아주신 정형빈 교수님께 감사 드립니다. 논문에 대한 유익한 말씀과 충고가 많은 도움이 되었습니다.

연구실에서 많은 시간을 함께했던 이한경, 박수진, 강건, 왕장운 선배, 동기 김은령 그리고 이제 연구를 시작한 배경량 후배의 많은 도움으로 석사과정을 잘 마무리 하게 되었습니다. 또한 다른 연구실에서 공부하지만 석사과정 동안 힘이 되어주고 많은 도움을 선후배분들과 동기

권희내, 최경민, 이유빈, 유림탁, 설병근께 감사 드립니다. 학교에서는 자주 만나지 못했지만 자주 연락하면서 힘이 되어준 임지현, 이윤정께 감사 드립니다. 그 외 많은 동기분들께도 감사 드립니다. 졸업하기까지 동기의 위로와 격려가 많은 도움이 되었습니다. 진심으로 감사 드립니다.

항상 저를 믿어주시고 묵묵히 응원해주시는 사랑하는 부모님께 감사 드립니다. 제멋대로인 딸인데 항상 이해해 주시고 믿어주셔서 제가 여기까지 할 수 있었습니다. 그리고 제 하소연을 항상 잘 들어주고 많은 격려와 힘을 준 장성빈씨께도 감사 드립니다. 덕분에 짧지만 긴 이 시간을 견뎌올 수 있었습니다.

이외에도 여기에 미처 적지 못한 많은 분들께 감사 드립니다. 여러분이 있어 제가 여기까지 올 수 있었고, 저도 여러분께 힘이 될 수 있도록 노력하겠습니다. 감사하고 사랑합니다.